Reflectivity and photoelectron yield from copper in accelerators

E. La Francesca,[1,2] M. Angelucci,[1] A. Liedl,[1] L. Spallino,[1] L. A. Gonzalez,[1,3]
I. Bellafont,[3,4] F. Siewert,[5] M. G. Sertsu,[5] A. Sokolov,[5] F. Schäfers,[5] and R. Cimino[1,*]

[1]*LNF-INFN, 00044 Frascati, Italy*
[2]*Università di Roma "La Sapienza", 00185 Rome, Italy*
[3]*CERN, CH-1211 Geneva, Switzerland*
[4]*ALBA Synchrotron Light Source, Barcelona, 08290 Spain*
[5]*Helmholtz-Zentrum-Berlin, 12489 Berlin, Germany*

For the design of high-performance particle accelerators and vacuum systems for high-energy colliders, the choice of materials and of their surface treatment is an essential prerequisite. Physical and optical properties of such materials and their coatings are input parameters for programs to simulate their performance and to validate machine design. Materials behavior after exposure to synchrotron radiation (SR), produced by the circulating particles, need to be studied because of its detrimental consequences, such as photo induced desorption, heat load, vacuum and beam induced instabilities. Reflectivity, its angular distribution and photo yield, i.e., the number of photoelectrons produced per incident photon, are essential ingredients to simulation codes. Such parameters must be studied not only on materials as they are in accelerators, but also in conditions as close as possible to the operative ones. In this work, we present results of such an experimental campaign, carried out at the Optics Beamline of BESSY-II. This experimental setup, designed to investigate quasiperfect x-ray-optical elements by "at-wavelength" metrology (from 35 eV to 1850 eV), is also an ideal tool to perform reflectivity and photo yield studies of vacuum chamber materials. As will be discussed, different roughness and various nano-, micro- or macro- modifications of a Cu-surface significantly influence the parameters under study. Energy- and angle-integrated values for the total reflectivity and photo yield are derived. Such integrated values are representative for material behavior under "white-light" irradiation for the various accelerators discussed here.

I. INTRODUCTION

The design of vacuum systems for present and future high-performance particle accelerators faces severe issues related to beam induced effects [1,2]. In particular, high energy accelerators for positively charged particles may incur into important limitations due to the emitted synchrotron radiation (SR) interacting with the vacuum chambers walls [1–15]. In accelerators using cold superconducting magnets the additional heat load deposited by SR will significantly affect the cryogenic budget, with direct impact to general costs and machine sustainability [9,11,12,16]. Moreover, in such machines, SR can produce additional gas desorption and photoelectrons with detrimental consequences to vacuum and beam stability [2]. SR induced photoelectrons may seed e^- cloud build-up if the materials secondary electron yield (SEY), i.e., the number of e^- produced per incident e^-, is high enough to cause their multiplication. All those e^- will interact with the (positive) beam and induce detrimental effects to it [1,2]. Since the first electron-cloud simulation for the LHC by F. Zimmermann in 1997 [17], there has been a significant effort to develop codes able to predict e^- cloud build-up and effects. Today the most used electron-cloud build-up codes are POSINST [18,19], ECLOUD [17,20], CLOUDLAND [21–23], and PyECLOUD [24–27]. Those codes implement different algorithms, based on theoretical or empirical models, for the production of primary and secondary electrons, but all of them use and benefit from material properties like SEY and photo yield as necessary input data. Photo yield (PY) is here defined as the number of e^- produced per incident photon and is also known as quantum efficiency. Even in absence of such e^- cloud build-up, the mere presence of a high density of electrons in the vacuum chamber has been shown to induce severe single-bunch instabilities on the machine performance [28,29]. To simulate single-beam instabilities and the seeding of e^- cloud build-up, it is not only essential to measure PY from real

materials under realistic conditions, but also to identify its spatial distribution. In a dipole, for example, all photo-electrons created in the orbit plane will be redeflected to it by the strong magnetic field and will not take part in any cloud build-up. Only photoelectrons created at the top and bottom of the vacuum vessel will interact with the beam and contribute to instabilities. Of course, the number of photo-electrons produced there will depend not only on the PY of the material but also on the number and energy of photons scattered/reflected on those parts. Therefore, the photon path along and its interaction with the beam pipe must be ray-traced systematically. For such studies data on the energy- and angle-dependent reflectivity (R) of the materials in question are required. Monte-Carlo computer codes, such as SYNRAD3D [10,30] and SYNRAD+ [8,13,14], are used to simulate SR-distributions in accelerator machines on the basis of any available experimental input parameter. Also vacuum simulations need detailed knowledge about R and PY [2]. Photon stimulated desorption (PSD) and electron stimulated desorption (ESD) calculations are based on those input parameters. PSD is the primary gas source also in electron synchrotrons. There, SR produces photoelectrons once hitting the vacuum chamber walls, and the electrons, in turn, release trapped gases from the surface into vacuum [15,31,32]. For this reason, our data can be useful also for electron machines when calculating vacuum properties. Once SR-distributions in accelerator machines are simulated, other programs like MOLFLOW [4] and MOLFLOW+ [13,14], will then calculate desorbed gas densities, heat load pro-files, etc.

During the LHC design and development, the SR, impedance and the e^- cloud related heat load on the cold bore have been significantly reduced by the introduction of a beam screen (BS) at higher temperatures (T $\approx$ 20 K) inside the cold bore [33]. The BS has to be compliant with many other functional requirements [31]. The inner hori-zontal Cu-surface, where the SR will first impinge, has been designed with a saw-tooth structure to reduce forward reflectivity [34]. The BS of LHC represents the starting point for the design and development of a new generation of high energy collider vacuum systems. Pushing forward the characteristics of these machines (energy, performance, size), may increase the impact of beam induced effects, requiring even more detailed studies of the relevant input parameters. For instance, the conceptual design of the Future Circular Collider (FCC)-hh [35] considers to accel-erate protons to reach an energy of 100 TeV in the center of mass operating with a 16 T dipole magnetic field. At the design energy, the proton beam emits an intense SR with critical energy (ϵ_c) as high as 4.5 keV. ϵ_c is defined as the photon energy that divides the emitted SR power in two equal parts [36]. These features enhance the design con-straints already present in the LHC. Reaching and main-taining, during operation, both the required very low temperatures (T $\approx$ 1.9 K) of the dipole walls, and the
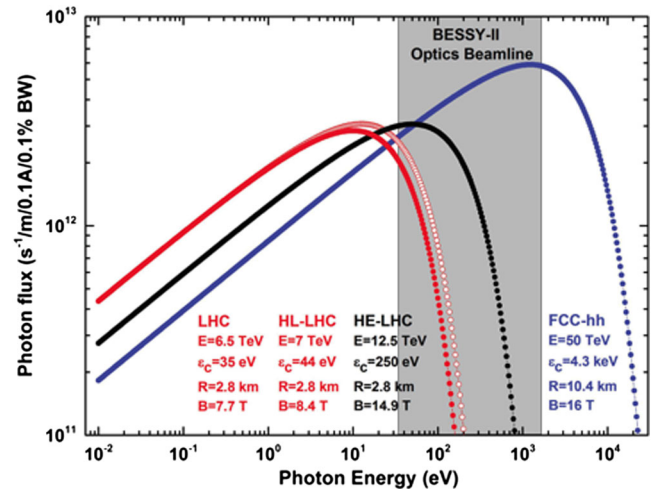

FIG. 1. Calculated SR flux and critical energies (ϵ_c) for nominal parameters of: LHC, HiLumi-LHC, HE-LHC and FCC-hh with 16 T dipole magnets.

necessary vacuum and beam stability, may be extremely difficult without a very careful and detailed study of all input parameters required to perform design validations [37]. Similar issues are also present in the design of the HE-LHC, which is a proposed machine to be built in the LHC tunnel using 16-20 T dipole magnets. Also for this case, even if the foreseen ϵ_c ranges between 500 and 800 eV, material studies are necessary to the design [38–40].

In Fig. 1 we report the calculated fluxes for the four colliders we plan to feed with useful realistic input parameters. Fluxes are calculated on the basis of the Schwinger-equations (bending magnet SR). The light is emitted into a vertical cone of $1/\gamma$ ($= m_{particle} \cdot c^2/E_{Ring}$) angular spread which corresponds to some pico- to nano-radian. The LHC emits primarily in the soft x-ray range, the FCC in the hard x-ray range, and HE-LHC is in between. Our accessible energy range is indicated. Here, we cover well the SR spectra of LHC and HE-LHC but not the higher energy part of the SR emitted by FCC-hh. Since photons of energies in the soft x-rays ($\leq$ 2 keV) have a higher cross section to produce photoelectrons and desorbed molecules, our data may be useful also for the FCC-hh case.

Detailed simulations of the different BS design are the tools to forecast the BS performance in terms of heat load, beam induced multipacting and molecular density behavior [5,10,14,16,29,39]. All the phenomena taken into account by the simulations need, as input parameters, reflectivity, photo yield, secondary electron yield, photon and electron stimulated gas desorption from real technical materials and their dependencies on photon energy and angle of inci-dence. Here, for technical surfaces, we mean a material that has undergone to the same production and cleaning treat-ments as the actual surface in the accelerator. As far as R and PY are concerned, very few and incomplete exper-imental data are available up to now [3,5–7,34,41–43].

Therefore, data on real technical samples measured in as close-as-possible operating condition, should become available and used as input parameters to obtain the necessary simulation accuracy. For this reason, we launched an experimental campaign to measure various technical surfaces in realistic geometry at the Optics beamline at BESSY-II. Soft x-ray reflectivity- and photo yield data on differently (either microscopically or macroscopically) prepared Cu-surfaces are presented and discussed. In the final section, we extrapolate from our data, angle- and energy-integrated reflectivity and photo yield. Those numbers allow a simplified approach to material properties under white-light irradiation for the different accelerators of interest.

II. EXPERIMENTAL

The Optics Beamline at BESSY-II is a dedicated SR laboratory for "at-wavelength" metrology of soft x-ray optical elements. Here, the reflectivity of a sample is measured as function of incidence angle and/or photon energy. Reflectometry is a very powerful nondestructive characterization technique for depth-profiling of microstructures, layered systems and buried layers [44–46]. There are various techniques for characterization of surface quality in terms of figure and finish of optical systems (atomic force microscopy (AFM), white light interferometry, x-ray diffraction and others). At-wavelength metrology represents the final test bench. The average spot-size at our samples was $\approx 0.2 \times 0.3$ mm^2 (FWHM, v x h), and the impinging beam has a divergence of 0.5 mrad $\times$ 3.6 mrad (v x h). These features are sufficient to avoid any significant increase of beam size, up to the detectors positioned 310 mm downstream the sample. All the reflected and most of the scattered radiation can therefore be detected by using the largest available photodiode (4.6×4.6 mm^2). The available energy range varies from 10 eV up to 2.0 keV. This range, even if it does not include all high energy photons emitted e.g., by FCC-hh (Fig. 1), is a wide and significant range for our purposes. To avoid spectral purity contamination due to unwanted presence of second or higher order radiation, we start most of our study at 35 eV. From that energy the beamline offers optical filters to minimize spurious radiation [46]. Therefore it allows us to obtain cleaner and more reliable data. At high energy, to minimize time and to work in a region with sufficiently high flux, we generally stop our scans at about 1850 eV. In any case, the spectral range at which the present experiments are performed is a significant improvement in respect to the up-to-now available data and extrapolation to higher/lower energy could be performed with some more confidence.

The end-station of the beamline is a versatile state-of-the-art UHV-Reflectometer, using four goniometers: for the sample azimuth and incidence angle setting and for the two-dimensional scanning of the detectors. The goniometers allow extremely precise angular positioning of both

sample and detector, and a very accurate alignment of their relative angles in respect to the incoming photon beam. This precision allows us to work at very small grazing incidence angles. The relevant incidence angles at LHC and FCC are $\sim 0.28°$ (4.8 mrad) and $\sim 0.08°$ (1.4 mrad) respectively. Let us underline here that the possibility to study surface properties upon photon irradiation in a geometry as close as possible to the real case, is one of the greatest benefits offered by the experimental setup at BESSY-II.

The reflectometer allows to measure PY along with all the reflectivity data. The sample under study is electrically insulated and connected to a Keithley picoammeter, which then measures the number of photoelectrons produced at the sample surface at a given photon energy and experimental geometry. No bias was applied not to add unwanted noise to the measurements. This may have caused a reduced PY signal due to eventual space charge effects, even if the electron current produced was quite small and distributed along the surface. The number of impinging photons is calculated multiplying the photodiode drain current by its tabulated energy-dependent quantum efficiency (GaAsP—G1127-02, Hamamatsu). Thus, the energy range and the geometrical conditions provided at the end station, guarantee the reliability of the obtained data and indicate the necessity of specialized experimental equipment for such benchmark experimental campaigns. Linearly polarized light was used throughout in s-reflection geometry (R = R$_s$).

For our experiments we define: (i) θ_i as the angle of incidence between the photon beam and the sample surface in the scattering plane. (ii) θ_r as the detector angle in the scattering plane. $\theta_r = 0$, when the detector measures the direct beam (I$_0$) without any sample. (iii) Φ as the detector off-plane angle defined as its angle with respect to the scattering plane.

The sample position is adjusted by an UHV-tripod system (six degrees of freedom) that allows the nano-metric fine alignment of the sample in respect to the incoming light. Downstream the sample a series of detectors with variable apertures is available for the various scopes.

Figure 2 shows the reflectivity from a quasiperfect Si-mirror (with a roughness of 0.2 nm rms), as function of the reflection angle, measured with an open detector (left) and with a detector having an entrance slit 0.25 mm (right). Obviously, angular sensitivity is required to distinguish specular from small- and wide angle scattering regions (right), while the angular integrating data (left) show a plateau as long as the reflected beam hits the photodiode. The logarithmic scale in Fig. 2 shows the available dynamic range. Scattering from a quasi-perfect mirror is in the 10^{-3}–10^{-5} range. This is totally different when analysing R of technical surfaces, which are far off optical quality. Even for the best "technical" surfaces, with minimal roughness and slope error, we are not able to individuate a clear reflected signal due to specular reflectivity. This is the reason why we somehow artificially define here as specular
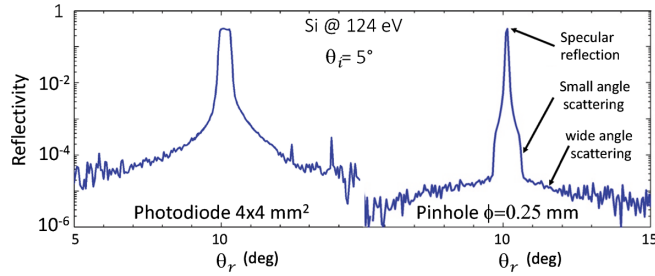
FIG. 2. Scattering from a quasi-perfect Si mirror surface taken at $\theta_i = 5°$ incidence angle and at 124 eV (10 nm). Data taken with an open 4.6×4.6 mm^2 photodiode (Left panel) and by the same detector masked by a circular pinhole with a diameter of $\Phi = 0.25$ mm [7].

FIG. 4. Picture of the inner part of the reflectometer. The sample is mounted on the tripod and can be precisely adjusted and rotated by θ. At 310 mm distance, a set of different photodiodes (detector) is mounted and can be rotated both in $\theta_r = 2\theta$ and Φ.

reflectivity R all the light entering the open photodiode, once it is centered at the geometrical reflection angle $\theta_r = 2\theta_i$. Therefore in this paper R comprises all the light emitted in a cone with an acceptance angle of 4/310 mm = 0.74° (12.9 mrad) both in θ_r and Φ direction. Total reflectivity R$_t$ is derived from integration over all solid angles.

Two measurement schemes were applied which are schematically shown in Fig. 3: (1) Specular reflectivity is obtained by the method described in the left panel. In a $\theta/2\theta$ scan the reflection angle is kept at $\theta_r = 2\theta_i$ and R is measured as function of incidence angle (at fixed photon energy) or photon energy (at fixed θ_i and θ_r). (2) Since, in general, the detector area (4×4 mm^2) was smaller than the reflected light cone from our technical surfaces, the total reflectivity had to be obtained by 2-D integration of angular resolved spectra. This is explained in the right panel of Fig. 3. At fixed photon energy and fixed incidence angle θ_i, the detector is scanned in the scattering plane (θ_r-scan) and/ or perpendicular to it (Φ-scan) to map the solid angle range.

A picture of the inner part of the reflectometer is shown in Fig. 4. A detector with an entrance slit of 4×0.1 mm^2 (h x v) was also used to achieve an angular resolution of 0.02°

(0.3 mrad) in the scattering direction. Such "slit detector" allows us to measure the actual reflected intensity distribution as function of θ_r. An example is reported in Fig. 5. There, we show the measured reflected intensity as function of θ_r for the case of LHC-Cu at 1800 eV and at fixed $\theta_i = 0.25°$. The acceptance angle of the "slitless detector" is also indicated. Integration in this slitless detector window will give the measured reflectivity R. The integration of R over the full ranges of θ_i and Φ available in our setup determines the total reflectivity R$_t$. With this procedure we could extract realistic estimates of R$_t$ for all samples, geometries and at some selected photon energies.

To get full use of the limited beamtime allocated to the experiment, we used to study total reflectivity R$_t$ by just considering a portion of the solid angle as long as the scattering intensity was above background level of the detector (10^{-13} A). Data were not collected in angular regions where the signal was comparable with the background and careful
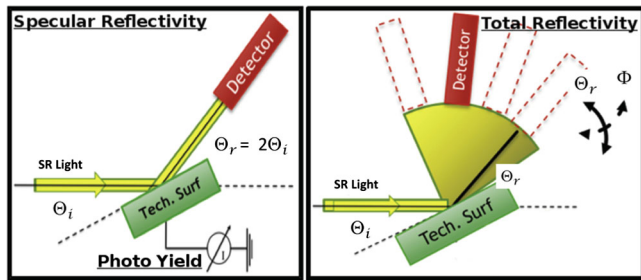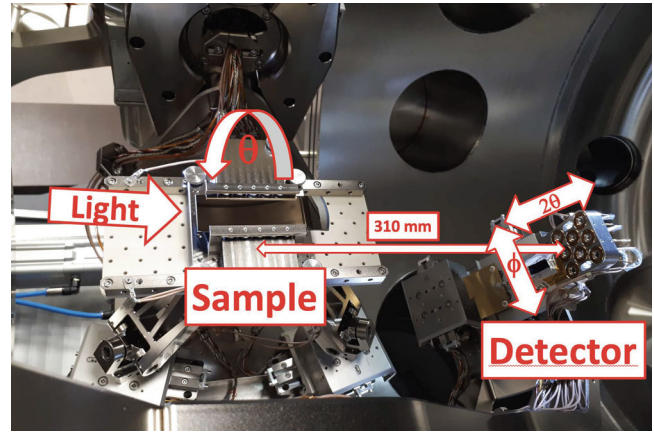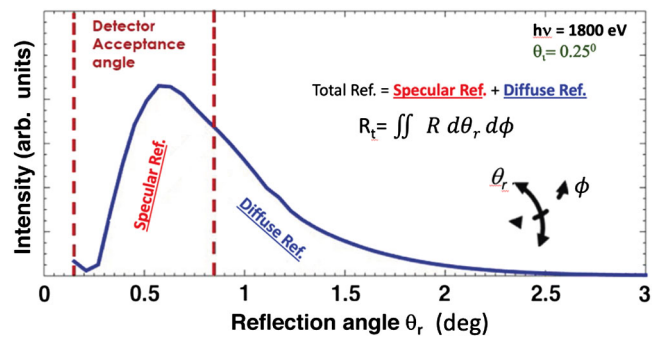

FIG. 3. Artistic view of the two adopted experimental configurations: (Left) The $\theta/2\theta$ geometry is used to measure R and PY. (Right) Measurement of angular distribution of reflected and scattered radiation keeping fixed the photon beam energy and the angle of incidence θ_i and by scanning the detector angle both in θ_r and Φ. Total reflectivity R$_t$ is derived by 2-D integration of the angular-resolved data.

FIG. 5. Angular resolved reflected intensity as function of θ_r for the Cu LHC sample (No. 4) taken at 1800 eV and at a fixed $\theta_i = 0.25°$ and $\Phi = 0°$. The slitless detector acceptance angle is shown. "Specular" and "diffuse" reflectivity regions are indicated. R$_t$ is obtained from integration over $d\theta_r$ $d\Phi$.

data analysis has been performed to avoid summing any artificial background to the R_t data. To additionally save acquisition time, the signal outside the scattering plane, at Φ unequal to 0°, has been acquired only for positive Φ and the result multiplied by two for symmetry reasons. In this way we can consider the measured R_t a close but lower estimate of the real R_t that would be obtained by full solid angle integration. As we will see from the data, R_t is, in some cases, as significant as the specular one. This is even more important since the measured R, as previously discussed, already contains a significant scattered signal added to the pure geometrical specular reflectivity. In all cases, the spot size, its optical aberration, the sample length and its slope error were defining the limiting angle at which all impinging photons were actually intercepting the sample surface. Given our focus size, this incidence angle is 0.25° and requires a sample length of at least 50 mm. Only in few distinguished cases, where the surfaces under study were sufficiently longer we could confidently reach 0.1°. Those cases, not shown here, confirm that, anyway, 0.25° is representative of the real accelerator scattering geometry. These data present a significant breakthrough to study material properties in realistic geometries.

III. SAMPLES

In the present work, we studied all the samples shown in Fig. 6, listed in Table I and described with some details in the following. Most of the different surface finishes could be obtained on a large industrial scale required in accelerator technology.

At first, we performed a detailed study on the importance of surface roughness (R_a) for otherwise "flat" technical surfaces. Therefore, we have selected four Cu-samples with different surface finish. The samples, named Cu 1A, Cu 1B, Cu 2A and Cu LHC, differ in their surface treatment and roughness, as reported in Table I. Their roughness values were determined by a $(20 \times 20 \ \mu m^2)$ AFM-measurement at various metrology laboratories active in our home institutions (HZB, CERN, INFN, and SBAI-Rome). A roughness variation from point to point was observed due to the nature of technical surfaces. Therefore we consider the AFM values to have an accuracy of $\pm 10\%$, which is significantly larger than the error bar given by a single AFM-measurement. In Fig. 6(b) we can also see two black strips due to a Carbon coating on Cu, which will not be discussed here, being outside the scope of this work. In addition to samples No. 1-4 we studied two other Cu-samples (No. 5, 6) after they were treated to significantly modify their surface morphology, either macroscopically or microscopically. Samples No. 5, 6 are potentially interesting materials that could be used for the construction of HL-LHC, HE-LHC and FCC-hh [2,12,15,16,33–35,37,39,47–50].

In particular we have analyzed: (i) No. 1-Cu 1A: a high finish flat polished copper sample, shown in Fig. 6(b); (ii) No. 2-Cu 2A: a medium finish flat polished copper
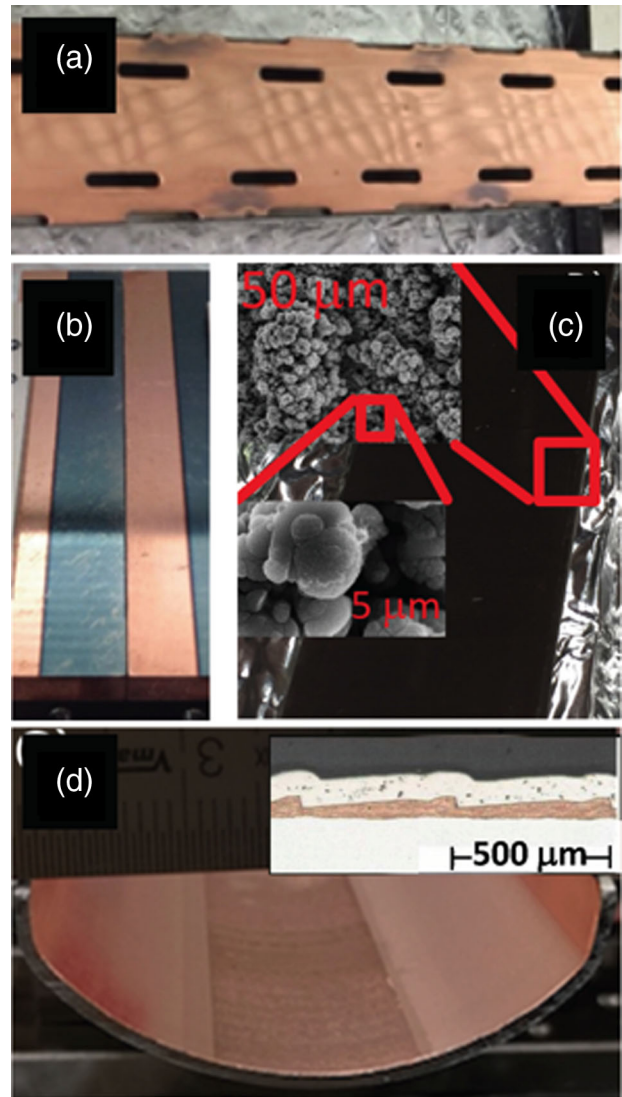

FIG. 6. Pictures of the investigated samples: (a) LHC flat Copper (Cu LHC—No. 4). (b) flat Copper (Cu 1A—No. 1 and Cu 1B—No. 3); (c) laser treated Copper (Cu-LASE—No. 6) with high resolution SEM images; (d) LHC Copper saw tooth (ST-LHC No. 5) [31,33].

sample, not shown; (iii) No. 3-Cu 1B: a medium finish flat lapped copper sample, shown in Fig. 6(b); (iv) No. 4-Cu LHC: LHC beam screen (BS), flat zone on top and bottom of the BS [31,33], shown in Fig. 6(a); (v) No. 5-ST-LHC: Copper LHC beam screen (BS), saw-tooth zone on the horizontal plane of the BS. It has been designed to be compliant with many functional requirements, one being the reduction of reflected photons reaching its top and bottom parts [31,33,34]. To this end a "saw-tooth" (ST) structure has been grooved into the 75 μm Cu-film during the co-lamination process. This resembles a blazed reflection grating profile with a line density of approximately two lines/mm and a blaze angle of 4.6, as shown in Fig. 6(d) and its inset. The direction of the grooves is approximately perpendicular to the reflection plane. The saw tooth profile

TABLE I. List of the investigated Cu-samples and some relevant parameters like pretreatment, roughness and secondary electron yield (see Fig. 6). Roughness data are from AFM.

No.	Sample	Material	Length (mm)	Treatment	R_a ±10%	δ_{max} ±10%
1	Cu 1A	Cu	100	el.-pol.	10 nm	2.2
2	Cu 2A			Degreased	27 nm	2.2
3	Cu 1B	Cu	100	Lapped Degreased	25 nm	2.2
4	Cu LHC	Cu	300	Co-lam. degreased	15 nm	2.2
5	ST-LHC	Cu	300	Co-lam. degreased	≈40 μ	2.25
6	Cu-LASE	Cu	300	laser treated. degreased	≈10 μ	≤ 0.75

is ~40 μm in height and ~500 μm in pitch, as shown in the inset of Fig. 6(d) and its upgraded replica is a potential candidate to be used in HL-LHC, HE-LHC and FCC-hh BS [15,35]. The data presented here are only accurate for the ST-LHC design and can be considered as indicative for other saw-tooth structures with different height/pitch and/or with different surface finish. ST-LHC is shown in Fig. 6(d) (vi) No. 6-Cu-LASE: Cu sample treated by Laser Ablation Surface Engineering [LASE, made by the Science & Technology Facility Council (STFC)] [47,48]. This treatment gives to the surface a particular morphology formed by different scale structures: micrometrical grooves with coral-like submicron agglomeration of nanospheres. These can be seen in the SEM zoomed images shown in Fig. 6C). This morphology is able to significantly reduce SEY [47,48] and is a potential candidate to be used in FCC-hh BS [49–51].

We show in Fig. 7 the secondary electron emission (δ) of the as received Cu-LHC (No. 4), of the ST-LHC (No. 5) and the LASE treated Cu-sample (No. 6) as measured in our Laboratory at LNF [1,52–56]. Due to the intrinsic inhomogeneity of all technical surfaces studied here, δ is
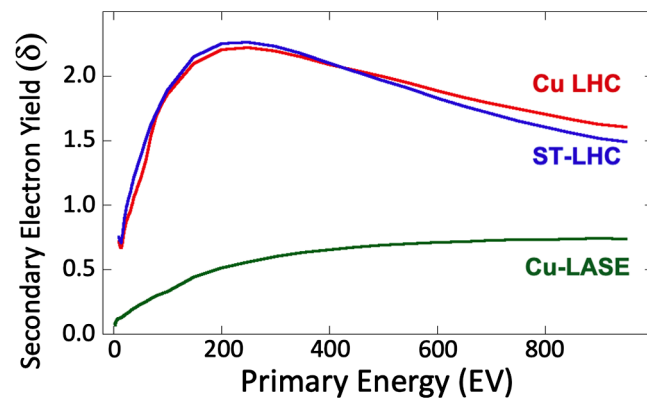

FIG. 7. Room temperature secondary electron yield (δ) of sample No. 1, 5, 6.

given with an error bar of ±10%, which is significantly larger than the one obtained by the single SEY measurement. While the first two samples, as expected and in agreement with literature results [1,52–56], do show very similar SEY with a maximum value of $\delta_{max} \approx 2.2$, the LASE shows the extremely interesting feature of a δ always less than unity as reported in the literature. [47,48]. Indeed this sample is particularly appealing for electron-cloud derived beam instabilities mitigation.

IV. RESULTS

To study the effect of surface roughness on R and PY, we first studied the four flat samples No. 1-4 (Cu 1A, Cu 1B, Cu 2A and Cu LHC) of Tab. I. From the measurements, it is possible to obtain their optical properties of interest. Once this is presented and discussed in detail, we will analyze the on-purpose modified Cu-surfaces No. 5 and No. 6 (ST-LHC and Cu-LASE). The selected results will be presented in the following as dedicates sub-sections, where the relevant data are separated by sample type and measured quantities, to improve readability. It is necessary to point out that simulation codes to compute R of x-ray optical elements such as REFLEC, RAY, IMD, CxRO and others [57–60], if used to simulate R of technical surfaces, give unrealistic results for two main reasons: (1) Roughness R_a is generally approximated as an attenuation parameter of the reflected intensity component (in REFLEC, for instance, as a Debye-Waller factor integrated with the Nevot-Croce formalism [61]). Such approximation is not really valid for the high R_a-values of technical surfaces, in particular at short wavelengths (i.e., high photon energies) and at very grazing angles of incidence, since scattering is not included in the codes. (2) It is very difficult to correctly consider the presence of contaminants and their effect, since their thickness and composition is unknown. This is particularly true for very grazing angles of incidence since, in this geometry R is strongly influenced by the topmost surface layers. Actually, the comparison between x ray reflectivity measurements and calculation from optical surfaces is indeed used to estimate the thickness and the composition of contaminant layers by a best fitting procedure. We attempted this extrapolation, but even for the sample with the smallest R_a, it was unsatisfactory. We hope to repeat such comparison between simulations and a Cu-flat sample with an optical finish surface ($R_a \le 0.5$ nm) to finally extract the R contribution from the contaminant layers. In this way, calculations might then be extrapolated to other geometrical configurations and the comparison with higher R_a samples will give us some hints on how relevant is roughness. Since our data are directly related to the samples studied, their general validity should only be considered as qualitative. For the time being, the inadequacy of existing simulation codes to correctly predict R for technical samples confirms that "at-wavelength"

metrology and dedicated experiments are, in fact, the only viable solution to obtain these values.

A. Flat Cu (Samples No. 1-4): Specular Reflectivity (R) vs energy

In Fig. 8 the experimental results of the specular reflectivity R are shown as a function of photon energy for three incidence angles ($\theta_i = 0.25°, 0.5°, 1°$) for the four "flat" Cu surfaces.

Looking at these data we see some main general aspects: (i) Specular reflectivity is higher at lower photon energies. (ii) Specular reflectivity is higher at lower angle of incidence θ_i. (iii) The Cu-$L_{2,3}$ absorption edge at ~932–953 eV is visible and causes a drop in R. (iv) In all spectra, in addition to the Cu-edge, we measure a significant effect due to the C K-edge at ~284 eV and O K-edge at ~543 eV, which are known to be present as surface contaminants. (v) C and O K-edges are more pronounced (and therefore, more effective) at smaller incidence angles. This is due to the decrease, into the bulk material, of the beam penetration depth. The dominance of such contaminant layer is therefore expected to be enhanced in FCC-hh, where the incidence angle can be as low as 0.08° [35]. The presence of C as contaminant is therefore expected to enhance R especially behind the Cu L-edge. (vi) Roughness, as expected, plays a major role in determining th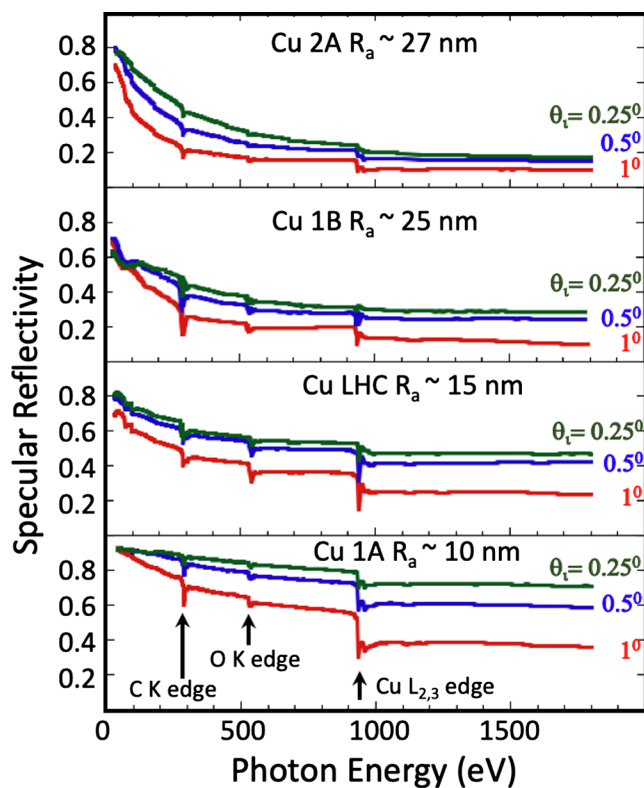e ability of a surface to specularly reflect impinging photons. For similar roughness (Cu 1B and Cu 2A) the type of surface treatment does not seem to significantly affect the reflectivity.

B. Flat Cu (Samples No. 1-4): Photo yield (PY) vs energy

Contemporary to the acquisition of the specularly reflected signal R, PY has been acquired and its dependence on the impinging photon energy and angle of incidence is presented in Fig. 9.

Also the PY data in Fig. 9 show a number of very interesting and general aspects: (i) PY is higher at higher photon energies. (ii) Generally, PY decreases with lower angle of incidence since R increases, hence the number of photons absorbed by the sample is reduced. However, this statement is only valid at angles lower than 1-2°, (total reflection regime), since, far from grazing incidence, the situation changes. In that case, more photons are absorbed in the bulk, in a depth larger than the electron mean free path. Therefore, the produced photoelectrons and their secondary cascade will not travel to the surface and contribute to PY. The existence of such two competing effects (photon penetration and R reduction) is more clearly visible in all the spectra collected at fixed photon energy and measured as function of angle, as briefly discussed in the next section. (iii) Roughness does influence the PY. The

FIG. 8. Specular reflectivity as a function of photon energy at incidence angles of 1°, 0.5°, 0.25° for Cu 1A, Cu LHC, Cu 1B, and Cu 2A sample (No. 1-4). R_a increases from bottom to top.
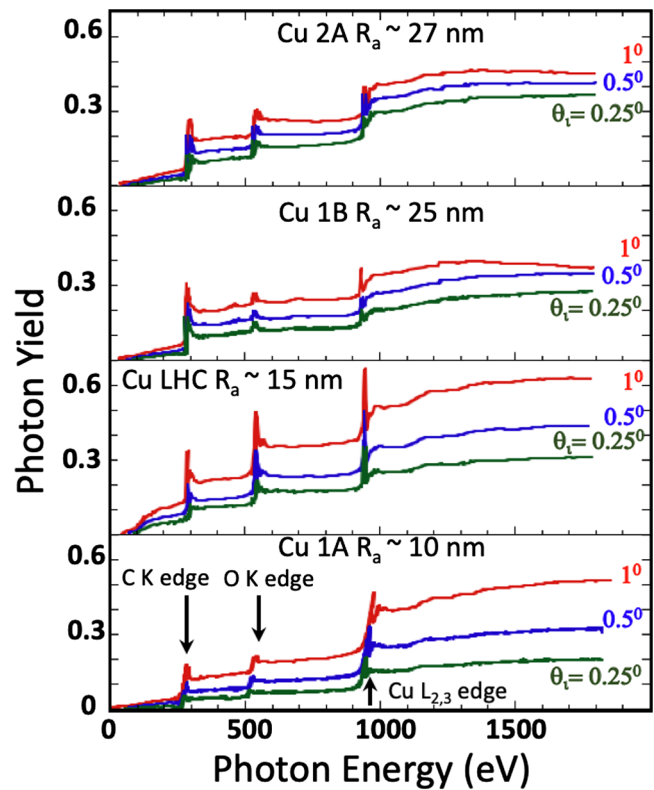
FIG. 9. Photo yield as a function of photon energy at incidence angles of 1°, 0.5°, 0.25° for Cu 1A, Cu LHC, Cu 1B, and Cu 2A sample (No. 1-4). R_a increases from bottom to top.

lower R_a, the higher PY. (iv) The PY-dependence on angle is consistently dimmed and finally washed out when the roughness increases. This can be qualitatively justified by the notion that with increasing R_a photons will hit the surface in a geometry which is locally similar for all angles. (v) In all cases, the Cu-$L_{2,3}$ absorption edge causes an increase in the measured PY. At any absorption edge, reflectivity drops and thus photoelectrons are produced. (vi) In all spectra, in addition to the Cu-edge, we measure a significant effect due to the C K-edge and O K-edge, which are present as surface contaminants. Also those edges enhance photoabsorption and hence PY.

It is important here to state that PY has been observed to decrease during photon irradiation [3,62] with a mechanism similar to the SEY reduction during electron irradiation [1,53,63]. Indeed, SEY and PY differ by the excitation particles (electron in one case and photons in the other) and in the geometry they are normally studied (near normal incidence in one case, close to very grazing incidence in the other). But, once the excitation particle has interacted with the solid, the two processes have great similarities and photon and electron scrubbing are mutually expected to act on PY and SEY in similar manner [3,62]. Of course this notion and its actual amount should be best verified with "ad-hoc" experiments.

C. Flat Cu LHC (Sample No. 4): R and PY vs angle

Another type of measurements, here presented only for the case of Cu LHC, is shown in Fig. 10. R and PY have been measured, as described in the experimental section, by $\theta/2\theta$ scans (see Fig. 3, left panel), as a function of the incidence angle θ_i, at seven photon energies. From the R data, shown in Fig. 10, panel (a), we can confidently confirm that the larger the photon energy, the lower will be the incidence angle at which R becomes strongly reduced.

For our sample, we see how high-energy photons, above 500 eV, are nearly completely absorbed at incidence angles
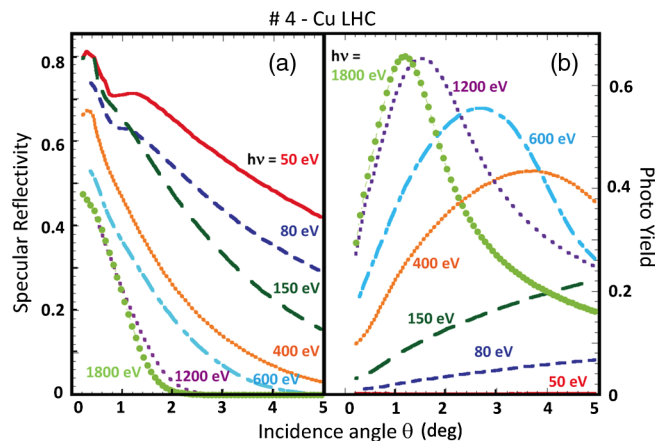
larger than two degrees. Low energy photons, on the contrary, are reflected considerably, up to almost 60% at 50 eV, up to large angles of incidence. This aspect highlights how many reflections low-energy photons can suffer before being finally adsorbed to create a photoelectron.

The PY-data in Fig. 10, panel (b) show the effect of the two conflicting processes: one derives from the fact that the more photons are reflected the less they are absorbed; the other derives form the different mean free paths of a photon and of an electron in a solid. For the first process, we clearly expect that PY increases with incidence angle, as it is observed at small angles. However, when the incidence angle becomes larger, photons will penetrate into the solid deeper than the escape depth of photoelectrons, implying that the photoelectrons produced will not escape from it and, therefore, will not contribute to PY. The angle at which the trade off between these two competing effects occurs, decreases with increasing photon energy. This is why we observe a maximum in PY which increases in angle at decreasing photon energies.

D. Flat Cu (Samples No. 1-4): Total reflectivity

To better understand why measuring total reflectivity is important, we performed various angular scan, of the type discussed in Fig. 5.

As an example, we show in Fig. 11 the angular resolved reflected intensity distribution over θ_r at 1800 eV for the four different Cu surfaces (No. 1-4). It is straightforward to notice how, with increasing roughness, the angular distribution broadens and decreases in intensity. The Cu 1A sample, with the lowest roughness, has a rather sharp angular distribution, with most of the signal within the acceptance angle cone of the slitless photodiode. In this case, the diffused light mostly suffers small angle scattering (see Fig. 2 and Fig. 5) and R is a measure for most of the reflected photons. If we follow the data in Fig. 11 in clockwise direction, from smallest to largest R_a, we see a

FIG. 10. Cu LHC specular reflectivity (a) and photo yield (b) as a function of the incidence angle θ_i at different photon energies.
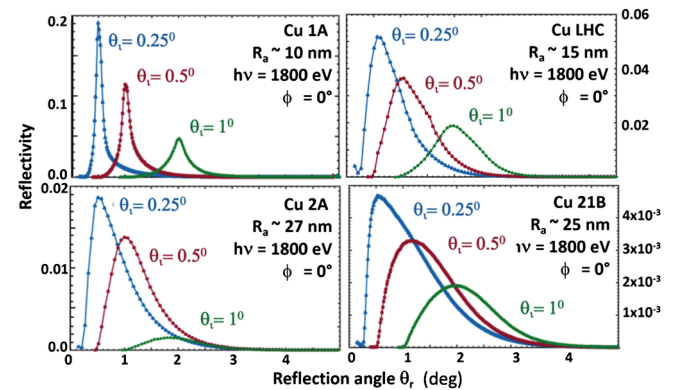
FIG. 11. Reflectivity vs reflection angle θ_r at 1800 eV at incidence angles of 1°, 0.5°, 0.25° for Cu 1A, Cu LHC, Cu 1B, and Cu 2A sample. Plots are ordered clockwise as sample R_a increases.
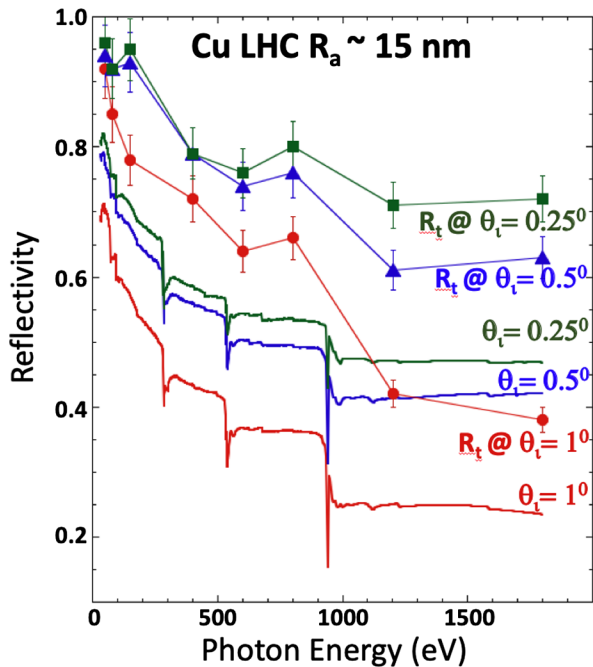
FIG. 12. Specular reflectivity R (curves taken from Fig. 8 and total reflectivity R_t as function of photon energy for the Cu-LHC flat sample (No. 4). R_t data were obtained by 2-D detector mapping and integration of the angular resolved measurements of Fig. 11 and many others (not shown).

TABLE II. Comparison between specular and total Reflectivity of Cu LHC sample No. 4 at eight photon energies for an incidence angle of 0.25°. R_t-data obtained by integration (Error estimate: $\Delta R/R = \pm 5\%$, $\Delta R_t/R_t = \pm 10\%$).

Photon energy (eV)	R Specular Reflectivity	R_t Total Reflectivity	Ratio R_t/R
1800	0.47	0.72	1.5
1200	0.47	0.71	1.5
800	0.53	0.80	1.5
600	0.54	0.76	1.4
400	0.59	0.79	1.3
150	0.71	0.95	1.3
80	0.75	0.92	1.2
50	0.81	0.96	1.2

TABLE III. Comparison between Specular (R) and Total (R_t) reflectivity for all Cu flat samples (No. 1 4) as a function of their roughness for $\theta_i = 0.25°$ and $h\nu = 1800$ eV. R_t-data obtained by integration (Error estimate: $\Delta R/R = 5\%$, $\Delta R_t/R_t = 10$).

Sample No.	Roughness R_a (nm)	R Specular Reflectivity	R_t Total Reflectivity	Ratio R_t/R
1	10	0.61	0.74	1.2
2	15	0.47	0.72	1.5
3	25	0.27	0.55	2.0
4	27	0.18	0.54	3.0

clear increase of the number of photons scattered at larger angles, and thus, an increasing contribution to the total reflectivity. Obviously, in those cases, the specular reflectivity R is not a valuable parameter to represent the number of reflected photons from a technical surface. Only measurements obtained by integration of all photons over a considerable portion of the solid angle can then give realistic input parameters for the total reflectivity from accelerator surfaces.

Due to the limited beamtime, the determination of R_t by integration of many angular-resolved measurements was done at selected energies only. A viable solution is shown in Fig. 12 for the most relevant case of the Cu LHC-flat surface. In addition to the specular reflectivity curves taken from Fig. 8, the R_t values obtained at eight photon energies are plotted. As described in the experimental section, such values have been obtained by scanning the slit-less diode over the chosen solid angle, without overlap and integrating the results.

The data in Fig. 12, which are partly tabulated in Tab. II, show the importance to measure R_t for the case of Cu LHC. The results of this comparison for all the flat copper surfaces as a function of their roughness is given in Table III for the smallest angle of incidence ($\theta_i = 0.25°$) and the highest available photon energy (1800 eV). Indeed, the measured R steadily decreases with increasing R_a, passing from about 0.6 for the smoother sample to 0.18 of the rougher one. Such significant decrease is not observed

in the R_t values, which changes only from 0.75 to 0.54. Data, not reported here, for lower energies confirm how R_t values are significant even in cases were the roughness is so high that nearly no specular reflectivity is expected. We show here, for the first time in this context, that with increasing R_a the geometrical reflectivity nearly vanishes (Fig. 5). We observe that the light scattered in specular direction remarkably decreases while R_t remains significant even at high photon energies. Thus, R_t is the relevant quantity to be used when studying reflectivity related properties at very grazing angle of incidence.

E. ST-LHC beam screen (Sample No. 5): R, PY, and R_t

Specular reflectivity (R) and the photo yield (PY) as function of photon energy for this ST- LHC are shown in the top and bottom panel of Fig. 13, respectively. In comparison to R measured from any flat Cu-sample studied here, this structure has a dramatically reduced R by more than two orders of magnitude, especially at photon energies higher than 50 eV, as evident in the top panel of Fig. 13. This phenomenon could be expected by extrapolating the observed dependence of R on roughness (Tables I and III). At very grazing incidence angle, the residual specular reflectivity R may be attributed to the "saw-tooth" crests, which are rounded by mechanical construction and still offer to the photons a minimal "close to grazing" surface
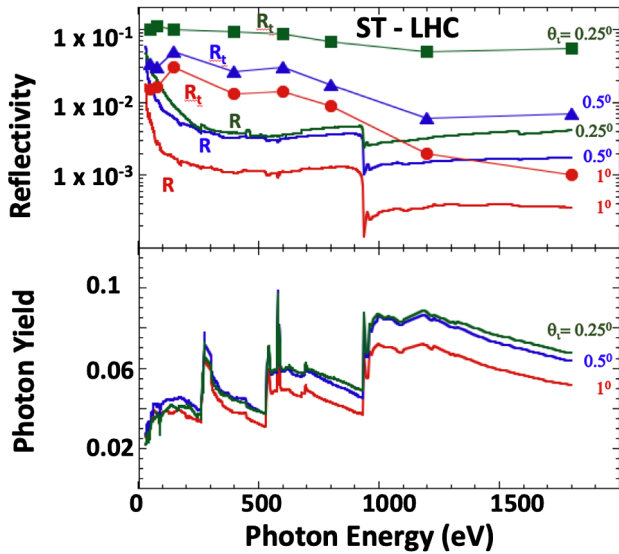
FIG. 13. Specular reflectivity R, total reflectivity R_t (top) and photo yield (bottom) as function of photon energy for three incidence angles for the ST-LHC sample No. 5. R_t data were obtained by 2-D detector mapping and integration of angular resolved measurements (not shown).

where to be forward scattered. Also the PY (shown in the bottom panel of Fig. 13) is reduced but only by a factor 10. The PY shows all the characteristic C and O K-, and Cu $L_{2,3}$ -edges as in all the other cases.

Due to its extremely large roughness, the large-angle scattering of this sample is considerably larger (not shown here). The comparison between specular and total reflectivity from this sample, shown in the top panel of Fig. 13, unambiguously shows the existence of a very significant amount of scattered light outside the geometrical reflectivity cone. However, off-plane scattering to angles $\Phi \gtrsim 2°$ was found to be negligible. The integration to obtain the R_t-values took into account nearly the full scattering plane up to $\theta_r \approx 175°$. The actual values, obtained for an incidence angle of 0.25° are reported in Table IV.

TABLE IV. Comparison between specular and total reflectivity for the ST-LHC sample No. 5 at eight photon energies of $\theta_i = 0.25°$. R_t-data obtained by integration (Error estimate: $\Delta R/R = 5\%$, $\Delta R_t/R_t = 10\%$).

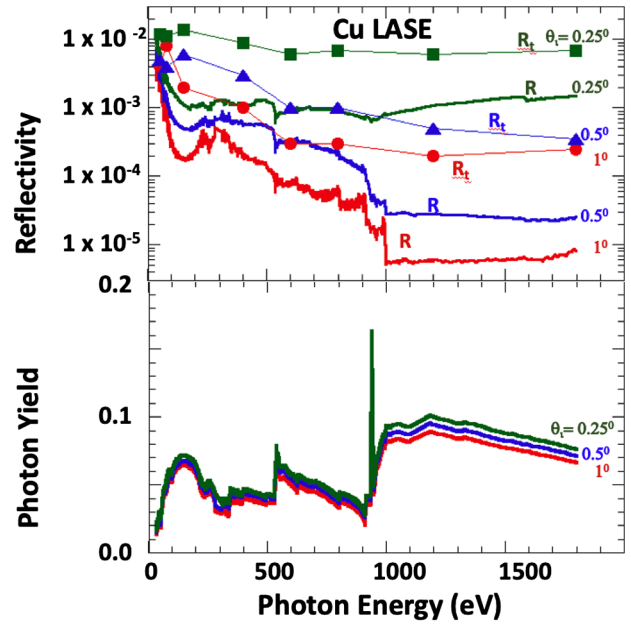| Photon energy (eV)	R Specular Reflectivity	R_t Total Reflectivity	Ratio R_t/R
1800	0.0004	0.05	12.5
1200	0.003	0.05	16.7
800	0.0045	0.07	25.6
600	0.0035	0.08	22.8
400	0.004	0.1	25
150	0.01	0.10	10
80	0.02	0.11	5.5
50	0.03	0.10	3.3

FIG. 14. Specular reflectivity R, total reflectivity R_t (top), and photo yield (bottom) as function of photon energy for three incidence angles for the Cu-LASE sample No. 6. R_t data were obtained by 2-D detector mapping and integration of angular resolved measurements (not shown).

F. Cu-LASE (Sample No. 6): R, PY, and R_t

This sample is a candidate material for the construction of the beam screen for FCC-hh, since its nanostructured surface grants a low secondary electron yield, hence it is promising to mitigate electron cloud related effects [15,32,47–50]. Its specular reflectivity and its photo yield as function of photon energy are shown in Fig. 14 top and
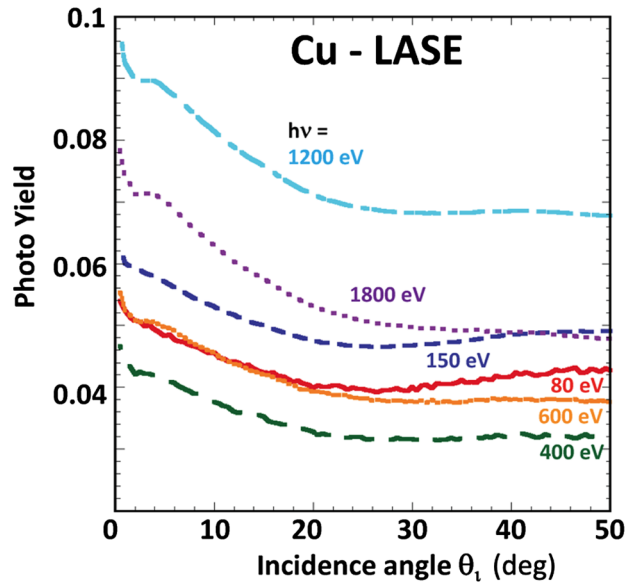

FIG. 15. Photo yield of the Cu-LASE sample No. 6 as function of incidence angle at selected photon energies.

TABLE V.   Comparison between specular and total reflectivity for the Cu-LASE sample No. 6 at eight photon energies for an incidence angle of $\theta_i = 0.25°$. R_t-data obtained by integration (Error estimate: $\Delta R/R = 10\%$, $\Delta R_t/R_t = -20/ + 100\%$).

Photon energy (eV)	R Specular Reflectivity	R_t Total Reflectivity	Ratio R_t/R
1800	0.0015	0.007	4.7
1200	0.0011	0.006	5.5
800	0.0009	0.007	7.8
600	0.0009	0.006	6.7
400	0.001	0.009	9
150	0.001	0.014	14
80	0.003	0.011	3.7
50	0.006	0.012	2

bottom panel, respectively. As expected, the extremely rough surface drastically reduces both reflectivity and photo yield. In both detection channels (and panels) of Fig. 14, the O K-edge shows up as surface contaminant, however, no measurable presence of Carbon appears, as previously observed by XPS as well [48].

The Cu-$L_{2,3}$-absorption is hard to see in Fig. 14, top panel, but it is evident in the PY data shown in Fig. 14, bottom panel. It is interesting to notice how the extremely large surface roughness significantly washes out most of the dependence on the angle of incidence from the PY signal, which stays nearly constant for all angles. This feature is confirmed by the data in Fig. 15, where the PY is shown at some selected photon energies and in a wider incidence angle interval.

Table V summarizes the measured and integrated reflectivity data given in Fig. 14, top panel for selected photon energies. It is remarkable how the intrinsic nature of the LASE surface can enhance the wide-angle scattering, such that in some cases R_t is up to 9- times larger than R. As for the other samples, the integration was done over the full reflection plane from $\theta_r = 0°$ to 175°. At variance with the ST-sample No. 5 just discussed, scattering from the LASE-sample may also be significantly distributed into the off-plane direction, i.e., at $\Phi \gg 0°$. Since, in our experiment, off-plane detector scanning is limited to $\Phi \leq \pm 2°$ we expect that the R_t-values may be systematically under-estimated. We therefore assign a larger relative error to the total reflectivity (see Table V).

V. DISCUSSION

All the experimental data on R, R_t, and PY, shown in the previous sections, do strongly depend on the photon energy and on the angle of incidence, which would be obvious for samples of x-ray optical quality. The results show that the optical behavior of our technical samples of poor surface quality follows, at least qualitatively, the same optical response. We have established an integration technique providing correction factors to take into account the much

stronger small- and wide-angle scattering due to the very rough nature of the surfaces. Thus at-wavelength metrology seems to be an adequate method to study such samples.

As mentioned before, such data are used as input parameters in various Monte-Carlo simulation codes for beam instabilities and vacuum behavior of an accelerator [1,2,4,8,10,13,14,17–30,32]. However, these codes require, in their present versions, single numbers for the energy- and angle-integrated reflectivity and photo yield. Thus, another simplification of our data must be provided, namely averaged white-light (WL)—values need to be extracted from them. These numbers have been obtained by con-voluting the SR spectra shown in Fig. 1 with the energy resolved R and PY. Such a simplification can be justified when analyzing the interaction of photons impinging for the first time (first hit), against the vacuum vessel. However, such mean values will loose their usefulness when raytracing scattering events after the "first hit". In fact, they will strongly depend not only on the machine WL-spectrum and geometry, but also on the energy range of the reflected photons and on their possibly different angle of incidence to "second hit", and even more to third and followings hits. Also, the shape of the vacuum vessel will eventually influence reflectivity, since curved surfaces may act and induce additional focussing or defocusing to the emerging beam [9]. This very complex multihit and multiparameter behavior can be addressed—if at all—by stochastical Monte-Carlo ray trace approaches with adequate boundary conditions.

In Fig. 1 we showed the synchrotron radiation spectra of the accelerators discussed here. In the next two sub-sessions, we derive approximate estimates of the relevant parameters studied for the various machines of interest, with the relevant exception of both FCC colliders. FCC-ee [29,64,65] has an extremely high energy SR emission (not shown in Fig. 1), since its ϵ_c ranges between 19.5 keV (for the so called "Z" version) and 1250 keV ("T" version). FCC-ee SR emission spectra are well above the photon energy range here studied, and the interaction of such high energy photons with matter should be studied on dedicated setups. The same applies for the FCC-hh ring with an ϵ_c of 4.5 keV [35], as shown in Fig. 1. Moreover the angle of incidence at which SR will impinge on the FCCs accel-erator wall is expected to be 0.08°, much less than our minimum angle (= 0.25°) at which measurements could be reliably performed. Other experiments, considerations or extrapolations of measured data to higher energies and/or smaller angles need to be performed to estimate the values for PY and R for those relevant cases. This discussion is outside the scope of the present paper.

A. The LHC and HL-LHC case

The critical energy ϵ_c for LHC (at 6.5 TeV) is 35 eV and for HL-LHC (at 7 TeV) is 44 eV, as reported in Fig. 1. The lower energy range (h$\nu \leq 35$ eV) was not accessible in our

TABLE VI. White-light (WL) $\bar{R}$, $\bar{R}_t$, and $\overline{PY}$-data for the cases of LHC and HL-LHC, averaged, from energy-resolved data, for an incidence angle of $\theta_i = 0.25°$. [Error estimate $\Delta\bar{R}/\bar{R}$, $\Delta\bar{R}_t/\bar{R}_t$, and $\Delta\overline{PY}/\overline{PY}$ in brackets (%)].

Sample No.	WL-Specular Reflectivity $\bar{R}$	WL-total Reflectivity $\bar{R}_t$	WL-Photo Yield $\overline{PY}$
1	0.9	0.95	0.03
	($\pm 10\%$)	($\pm 10\%$)	($\pm 10\%$)
2	0.5	0.85	0.07
	($\pm 10\%$)	($\pm 10\%$)	($\pm 10\%$)
3	0.6	0.85	0.07
	($\pm 10\%$)	($\pm 10\%$)	($\pm 10\%$)
4	0.7	0.9	0.07
	($\pm 10\%$)	($\pm 10\%$)	($\pm 10\%$)
5	0.01	0.1	0.04
	($\pm 30\%$)	($\pm 50\%$)	($\pm 10\%$)
6	0.002	0.01	0.05
	($\pm 30\%$)	($-20/+100\%$)	($\pm 10\%$)

TABLE VII. White-light (WL) $\bar{R}$, $\bar{R}_t$, and $\overline{PY}$-data for the case HE-LHC, averaged, from energy-resolved data, for an incidence angle of $\theta_i = 0.25°$. [Error estimate $\Delta\bar{R}/\bar{R}$, $\Delta\bar{R}_t/\bar{R}_t$, and $\Delta\overline{PY}/\overline{PY}$ in brackets (%)].

Sample No.	WL-Specular Reflectivity $\bar{R}$	WL-total Reflectivity $\bar{R}_t$	WL-Photo Yield $\overline{PY}$
1	0.85	0.9	0.1
	($\pm 10\%$)	($\pm 10\%$)	($\pm 10\%$)
2	0.45	0.8	0.15
	($\pm 10\%$)	($\pm 10\%$)	($\pm 10\%$)
3	0.5	0.8	0.2
	($\pm 10\%$)	($\pm 10\%$)	($\pm 10\%$)
4	0.60	0.85	0.2
	($\pm 10\%$)	($\pm 10\%$)	($\pm 10\%$)
5	0.008	0.08	0.05
	($\pm 30\%$)	($\pm 50\%$)	($\pm 10\%$)
6	0.002	0.02	0.06
	($\pm 50\%$)	($-20/+100\%$)	($\pm 10\%$)

experiment. While, generally, the lower the photon energy the higher the reflection probability, the lower will be their PY. Therefore our estimates for WL-$\bar{R}$ and WL-$\bar{R}_t$ are the low limits, for WL-$\overline{PY}$ it is the high limit. The angle of incidence here studied (0.25°) matches the real one in LHC and its HL-upgrade (0.27°) and therefore the averaged data $\bar{R}$, $\bar{R}_t$, and $\overline{PY}$ presented in Table VI are, with respect to this, representative, at least for the "first hit".

Our data confirm the very strong dependence of R on incidence angle. This gives a strong warning when using the average value of $\bar{R}$ extracted from data taken at = 0.27° also for calculating multiple reflections. In that case, especially for high roughness surfaces, and, even more, for modified surfaces like ST-Cu and LASE, the spread in the scattering angles (as confirmed by the very strong difference between R and R_t) is extremely significant and input parameters to simulate subsequent multiple reflections must be evaluated with great care. The PY, on the other hand, loses its θ_i-dependence the rougher the surface is. To correctly evaluate PY generated by subsequent reflections, therefore it will not be necessary to analyze the angular dependence but to consider its spectral distribution.

B. The HE-LHC case

The HE-LHC is an upgrade-proposal of LHC in the existing 27 km tunnel with 16 T bending magnets [38–40]. Its critical energy ϵ_c is 550 eV (Fig. 1), well within our investigated photon energy range. Also the incidence angles studied matches the actual one (0.27°). Even though the low- (≤ 35 eV) and high-energy regions (≥ 1850 eV) were inaccessible in our experiment, our best estimates for White-Light $\bar{R}$, $\bar{R}_t$ and $\overline{PY}$ given in Table VII will not be significantly affected by these missing ranges. Again, the table data are only representative for the "first hit". They are

not valid for multiple reflections, since, also in this case the mean values should be obtained not only by mediating over the energy range, but also over the angular range.

VI. CONCLUSION

Experiments at the BESSY-II Optics Beamline allow the soft x ray-optical characterization of different Cu-samples currently used and foreseen to be used in accelerators. The saw-tooth and laser treated Cu-surfaces are of special interest for the design of LHC, HL-LHC, HE-LHC, and FCC-hh beam screens. The reflectivity and photo yield of Cu-samples of various microscopic roughness and macroscopic surface treatment have been measured in the photon energy region between 35 eV and 1850 eV. By this characterization, parameters essential for their application, such as their reflectivity and photo yield, were extracted. Such results were obtained for the first time very close to operational and geometrical conditions (incidence angle, energy range). The results presented here are now available as input for simulation codes used to study and validate the design and performance of present and planned accelerator machines. We mention all the warnings relative to their uses in realistic cases. Our experimental approach and the setup, which is normally used to investigate x-ray optical surfaces, have been validated and confirmed to be well suited to study technical materials as well. Our data clearly show the importance of measuring and considering the reflectivity to correctly simulate quantities related to the unavoidable existence of SR in an accelerator. At the very low angles of incidence considered here and at the typical roughness of technical surfaces, most programs to calculate reflectivity on the basis of Fresnel equations give significantly reduced values, as confirmed by our data. We have reported here clear evidence that not only small-angle scattering occurs, but also an even more significant number of large angle

scattered photons will irradiate the accelerator walls. On the experimental side, this study could be extended to other surface coatings, treatments, energy ranges and geometries. Also, one has to understand and quantify the effects of long exposure to synchrotron light (photo irradiation) and if and how this may modify measured parameters of relevance.

---

[1] R. Cimino and T. Demma, Electron cloud in accelerators, Int. J. Mod. Phys. A **29,** 1430023 (2014).

[2] O. Malyshev, *Vacuum in Particle Accelerators: Modelling, Design and Operation of Beam Vacuum Systems* (Wiley, New York, 2019), ISBN 9783527809165, https://books.google.it/books?id=Dgm5DwAAQBAJ.

[3] R. Cimino, I. R. Collins, and V. Baglin, VUV photoemission studies of candidate Large Hadron Collider vacuum chamber materials, Phys. Rev. Accel. Beams **2,** 063201 (1999).

[4] R. Kersevan, Monte Carlo calculations of pressure profiles in particle accelerator storage rings, in *51st IUVSTA Workshop: Workshop on Modern Problems and Capability of Vacuum Gas Dynamics* (2007), http://lss.fnal.gov/conf/C070709.13/Kersevan.pdf.

[5] L. Boon and K. Harkay, Chamber surface roughness and electron cloud for the advanced photon source superconducting undulator, in *Proceedings of ECLOUD'12* (2013); Report No. CERN-2013-002, p. 95, https://doi.org/10.5170/CERN-2013-002.95.

[6] L. Boon, J. Crittenden, K. Harkay, and T. Ishibashi, Application of the SYNRAD3D photon-tracking model to shielded pickup measurements of electron cloud buildup at CesrTA, in *Proceedings of the 2nd International Particle Accelerator Conference, San Sebastián, Spain* (EPS-AG, Spain, 2011), WEPC141, p. 2319.

[7] F. Schäfers and R. Cimino, Soft X-ray reflectivity: from quasi-perfect mirrors to accelerator walls, in *Proceedings*

[8] of ECLOUD'12* (2013); Report No. CERN-2013-002, p. 105, https://doi.org/10.5170/CERN-2013-002.105.

[8] M. Ady and R. Kersevan, Introduction to the latest version of the test-particle Monte Carlo code molflow, in *Proceedings, IPAC 2014* (2014), Vol. WEPME038, p. 2348, http://jacow.org/IPAC2014/papers/wepme038.pdf.

[9] R. Cimino, V. Baglin, and F. Schäfers, Potential Remedies for the High Synchrotron-Radiation-Induced Heat Load for Future Highest-Energy-Proton Circular Colliders, Phys. Rev. Lett. **115,** 264804 (2015).

[10] G. F. Dugan, K. G. Sonnad, R. Cimino, T. Ishibashi, and F. Schäfers, Measurements of x-ray scattering from accelerator vacuum chamber surfaces, and comparison with an analytical model, Phys. Rev. Accel. Beams **18,** 040704 (2015).

[11] G. Apollinari, I. B. Alonso, O. Brüning, M. Lamont, and L. Rossi, *High-Luminosity Large Hadron Collider (HL-LHC): Preliminary Design Report*, CERN Yellow Reports: Monographs (CERN, Geneva, 2015), https://doi.org/10.5170/CERN-2015-005.

[12] G. Apollinari, I. B. Alonso, O. Brüning, P. Fessia, M. Lamont, L. Rossi, and L. Tavian, *High-Luminosity Large Hadron Collider (HL-LHC): Technical Design Report V. 0.1*, Vol. 4 of CERN Yellow Reports: Monographs (CERN, Geneva, 2017), https://doi.org/10.23731/CYRM-2017-004.

[13] M. Ady, Monte Carlo simulations of ultra high vacuum and synchrotron radiation for particle accelerators, Ph.D. thesis, EPFL—Lausanne, Lausanne (2016), http://infoscience.epfl.ch/record/221165.

[14] R. Kersevan and M. Ady, Recent developments of Monte-Carlo codes Molflow+ and Synrad+, 10th International Particle Accelerator Conference, Melbourne, Australia, 19 - 24 May 2019, TUPMP037, 1327 (2019), http://cds.cern.ch/record/2694236.

[15] I. Bellafont, M. Morrone, L. Mether, J. Fernández, R. Kersevan, C. Garion, V. Baglin, P. Chiggiato, and F. Pérez, Design of the future circular hadron collider beam vacuum chamber, Phys. Rev. Accel. Beams **23,** 033201 (2020).

[16] F. Zimmermann *et al.*, Beam-dynamics issues in the FCC, in *Proceedings, 57th ICFA Advanced Beam Dynamics Workshop on High-Intensity and High-Brightness Hadron Beams (HB2016)* (2016), Vol. WEAM5X01, p. 101, https://doi.org/10.18429/JACoW-HB2016-WEAM5X01.

[17] F. Zimmermann, A simulation study of electron-cloud instability and beam-induced multipacting in the LHC, CERN LHC Project Report 95, 1997.

[18] M. A. Furman and G. R. Lambertson, The electron-cloud instability in PEP-II, in *Proceedings of the International Workshop on Multibunch Instabilities in Future Electron and Positron Accelerators "MBI-97"*, edited by Y. H. Chin, KEK Proceedings No. 97-17 (KEK, Tsukuba, Japan, 1997).

[19] M. A. Furman and M. F. Pivi, Probabilistic model for the simulation of secondary electron emission, Phys. Rev. Accel. Beams **5,** 124404 (2002).

[20] G. Rumolo and F. Zimmermann, Practical user guide for ECloud, CERN Report No. SL-Note-2002-016, 2002, see also The ECLOUD Program, http://wwwslap.cern.ch/collective/electron-cloud/Programs/Ecloud/ecloud.html.

[21] L. F. Wang, H. Fukuma, K. Ohmi, S. Kurokawa, K. Oide, and F. Zimmermann, Numerical study of the photoelectron cloud in KEKB Low Energy Ring with a three-dimensional particle in cell method, Phys. Rev. Accel. Beams **5,** 124402 (2002).

[22] L. F. Wang, H. Fukuma, K. Ohmi, S. Kurokawa, K. Oide, and F. Zimmermann, 3D simulation of photoelectron cloud in KEKB LER, in *Proceedings of ECLOUD'02* (2013), p. 113, https://doi.org/10.5170/CERN-2002-001.113; Report No. CERN-2002-001.

[23] L. Wang, User's guide for CLOUDLAND, KEK Internal Report No. 2003-2, 2003.

[24] G. Iadarola, G. Arduini, V. Baglin, H. Bartosik, J. E. Muller, G. Rumolo, L. Shaposhnikova, E. Tavian, F. Zimmermann, O. Domnguez, and G. H. I. M. Cuna, Electron cloud and scrubbing studies for the LHC, in *Proceedings of the 4th International Particle Accelerator Conference, IPAC-2013, Shanghai, China, 2013* (JACoW, Shanghai, China, 2013), p. 1131.

[25] G. Iadarola and G. Rumolo, PyECLOUD and build-up simulations at CERN, in *Proceedings of ECLOUD'12* (2013); Report No. CERN-2013-002, p. 189.

[26] G. Iadarola, Electron cloud studies for CERN particle accelerators and simulation code development, Ph.D. thesis, U. Naples (main) (2014), http://cds.cern.ch/record/1705520?ln=en.

[27] G. Iadarola, E. Belli, K. Li, L. Mether, A. Romano, and G. Rumolo, Evolution of python tools for the simulation of electron cloud effects, in *Proceedings of IPAC'17—THPAB043-*, 2017, CERN-ACC-2017-240, p. 3803, https://cds.cern.ch/record/2289165.

[28] K. Ohmi and F. Zimmermann, Head-Tail Instability Caused by Electron Clouds in Positron Storage Rings, Phys. Rev. Lett. **85,** 3821 (2000).

[29] K. Ohmi, L. Mether, D. Schulte, and F. Zimmermann, Study of electron cloud instabilities in FCC-hh, in *Proc. 6th Int. Particle Accelerator Conf. (IPAC'15), Richmond, VA, USA, May 2015*, pp. 2007–2009, https://doi.org/10.18429/JACoW-IPAC2015-TUPTY006.

[30] G. F. Dugan and D. Sagan, SYNRAD3D photon propagation and scattering simulations, in *Proceedings of ECLOUD'12* (2013); Report No. CERN-2013-002, p. 117, https://doi.org/10.5170/CERN-2013-002.117.

[31] V. Baglin, P. Lebrun, L. Tavian, and R. van Weelderen, Cryogenic beam screens for high-energy particle accelerators, CERN Technical Report No. CERN-ATS-2013-006, 2013, https://cds.cern.ch/record/1507613.

[32] I. Bellafont, R. Kersevan, and L. Mether, Summary of modelling studies on the beam induced vacuum effects in the FCC-hh, in 10th International Particle Accelerator Conference, Melbourne, Australia, 19 - 24 May 2019, p. TUPMP038, https://cds.cern.ch/record/2694056.

[33] S. Myers, The large hadron collider 2008–2013, Int. J. Mod. Phys. A **28,** 1330035 (2013).

[34] N. Mahne, V. Baglin, I. Collins, A. Giglia, L. Pasquali, M. Pedio, S. Nannarone, and R. Cimino, Photon reflectivity distributions from the LHC beam screen and their implications on the arc beam vacuum system, Appl. Surf. Sci. **235,** 221 (2004), ISSN , 8th European Vacuum Conference

and 2nd Annual Conference of the German Vacuum Society.

[35] A. Abada, M. Abbrescia, S. AbdusSalam *et al.*, FCC-hh: The hadron collider, Eur. Phys. J. Spec. Top. **228,** 7551107 (2019).

[36] J. D. Jackson, *Classical Electrodynamics* (Wiley Eastern Limited, New York, 1975).

[37] L. A. Gonzalez, M. Gil-Costa, V. Baglin, P. Chiggiato, C. Garion, R. Kersevan, S. Casalbuoni, E. Huttel, I. Bellafont, and F. Pérez, Commissioning of a beam screen test bench experiment with a future circular hadron collider type synchrotron radiation beam, Phys. Rev. Accel. Beams **22,** 083201 (2019).

[38] F. Zimmermann, HE-LHC overview, parameters and challenges, ICFA Beam Dyn. Newsl. **72,** 138 (2017), https://cds.cern.ch/record/2315725.

[39] F. Zimmermann *et al.*, Updated high-energy LHC design, in 10th International Particle Accelerator Conference, Melbourne, Australia, 19–24 May 2019, https://cds.cern.ch/record/2695084.

[40] A. Abada, M. Abbrescia, S. AbdusSalam *et al.*, HE-LHC: The high-energy large hadron collider, Eur. Phys. J. Spec. Top. **228,** 1109 (2019).

[41] V. Baglin, I. R. Collins, O. Gröbner, C. Grünhagel, B. Henrist, N. Hilleret, and B. Jenninger, Measurements at EPA of vacuum and electron-cloud related effects, in *Proceedings of Chamonix XI* (CERN, Geneva, 2001); Report No. CERN-SL-2001-003 DI.

[42] R. Cimino, V. Baglin, and I. R. Collins, VUV synchrotron radiation studies of candidate LHC vacuum chamber materials, Vacuum **53,** 273 (1999).

[43] F. Schäfers and R. Cimino, Soft X-ray reflectivity and photoelectron yield of technical materials: Experimental input for instability simulations in high intensity accelerators, in *Proc. 5th Int. Particle Accelerator Conf. (IPAC'14), Dresden, Germany, June 2014*, pp. 2335–2337, https://doi.org/10.18429/JACoW-IPAC2014-WEPME034.

[44] A. A. Sokolov, F. Eggenstein, A. Erko, R. Follath, S. Künstner, M. Mast, J. S. Schmidt, F. Senf, F. Siewert, T. Zeschke, and F. Schäfers, An XUV optics beamline at BESSY II, in *Advances in Metrology for X-Ray and EUV Optics V*, edited by L. Assoufid, H. Ohashi, and A. K. Asundi, International Society for Optics and Photonics (SPIE, 2014), Vol. 9206, pp. 138–150, https://doi.org/10.1117/12.2061778.

[45] A. Sokolov, P. Bischoff, F. Eggenstein, A. Erko, A. Gaupp, S. Künstner, M. Mast, J.-S. Schmidt, F. Senf, F. Siewert *et al.*, At-wavelength metrology facility for soft X-ray reflection optics, Rev. Sci. Instrum. **87,** 052005 (2016).

[46] A. Sokolov, M. G. Sertsu, A. Gaupp, M. Lüttecke, and F. Schäfers, Efficient high-order suppression system for a metrology beamline, J. Synchrotron Radiat. **25,** 100 (2018).

[47] R. Valizadeh, O. B. Malyshev, S. Wang, S. A. Zolotovskaya, W. A. Gillespie, and A. Abdolvand, Low secondary electron yield engineered surface for electron cloud mitigation, Appl. Phys. Lett. **105,** 231605 (2014).

[48] R. Valizadeh, O. Malyshev, S. Wang, T. Sian, M. Cropper, and N. Sykes, Reduction of secondary electron yield for

E-cloud mitigation by laser ablation surface engineering, Appl. Surf. Sci. **404**, 370 (2017), ISSN .

[49] S. Calatroni, E. G.-T. Valdivieso, H. Neupert, V. Nistor, A. T. Fontenla, M. Taborelli, P. Chiggiato, O. Malyshev, R. Valizadeh, S. Wackerow *et al.*, First accelerator test of vacuum components with laser-engineered surfaces for electron-cloud mitigation, Phys. Rev. Accel. Beams **20**, 113201 (2017).

[50] S. Calatroni, E. G.-T. Valdivieso, A. T. P. Fontenla, M. Taborelli, H. Neupert, M. Himmerlich, P. Chiggiato, D. Bajek, S. Wackerow, and A. Abdolvand, Optimization of the secondary electron yield of laser-structured copper surfaces at room and cryogenic temperature, Phys. Rev. Accel. Beams **23**, 033101 (2020).

[51] L. Spallino, M. Angelucci, R. Larciprete, and R. Cimino, On the compatibility of porous surfaces with cryogenic vacuum in future high-energy particle accelerators, Appl. Phys. Lett. **114**, 153103 (2019).

[52] R. Cimino, I. R. Collins, M. A. Furman, M. Pivi, F. Ruggiero, G. Rumolo, and F. Zimmermann, Can Low-Energy Electrons Affect High-Energy Physics Accelerators?, Phys. Rev. Lett. **93**, 014801 (2004).

[53] R. Cimino, M. Commisso, D. R. Grosso, T. Demma, V. Baglin, R. Flammini, and R. Larciprete, Nature of the Decrease of the Secondary-Electron Yield by Electron Bombardment and its Energy Dependence, Phys. Rev. Lett. **109**, 064801 (2012).

[54] R. Larciprete, D. R. Grosso, M. Commisso, R. Flammini, and R. Cimino, Secondary electron yield of Cu technical surfaces: Dependence on electron irradiation, Phys. Rev. Accel. Beams **16**, 011002 (2013).

[55] R. Cimino, L. A. Gonzalez, R. Larciprete, A. Di Gaspare, G. Iadarola, and G. Rumolo, Detailed investigation of the low energy secondary electron yield of technical Cu and its relevance for the LHC, Phys. Rev. Accel. Beams **18**, 051002 (2015).

[56] L. A. Gonzalez, M. Angelucci, R. Larciprete, and R. Cimino, The secondary electron yield of noble metal surfaces, AIP Adv. **7**, 115203 (2017).

[57] F. Schäfers, *Modern Developments in X-Ray and Neutron Optics* (Springer, Berlin, Heidelberg, 2008), Vol. 137, ISBN 978-3-540-74560-0.

[58] B. Henke, E. Gullikson, and J. Davis, X-ray interactions: Photoabsorption, scattering, transmission, and reflection at $E = 50$–30,000 eV, $Z = 1$–92, At. Data Nucl. Data Tables **54**, 181 (1993), ISSN .

[59] D. L. Windt, IMD–Software for modeling the optical properties of multilayer films, Comput. Phys. **12**, 360 (1998).

[60] CXRO X-Ray Interactions With Matter:, http://henke.lbl.gov/optical_constants/.

[61] L. Névot and P. Croce, Caractérisation des surfaces par réflexion rasante de rayons X. Application à l'étude du polissage de quelques verres silicates, Rev. Phys. Appl. (Paris) **15**, 761 (1980).

[62] M. Angelucci and R. Cimino, Synchrotron radiation studies of relevance to Accelerator R&D, in *Proceedings of the XXVII Meeting of the Italian Synchrotron Radiation Society* (Springer, New York, 2020), SILS2019—Springer volume.

[63] N. Hilleret, C. Scheuerlein, and M. Taborelli, The secondary-electron yield of air-exposed metal surfaces, Appl. Phys. A **76**, 1085 (2003).

[64] M. Benedikt, A. Blondel, P. Janot, M. Klein, M. Mangano, M. McCullough, V. Mertens, K. Oide, W. Riegler, D. Schulte *et al.*, Future circular colliders, Annu. Rev. Nucl. Part. Sci. **69**, 389 (2019).

[65] A. Abada, M. Abbrescia, S. AbdusSalam *et al.*, FCC-hh: The hadron collider, Eur. Phys. J. Spec. Top. **228**, 755 (2019).